ACS APPLIED MATERIALS & INTERFACES

Research Article

www.acsami.org

Controllable Tailoring Graphene Nanoribbons with Tunable Surface Functionalities: An Effective Strategy toward High-Performance Lithium-Ion Batteries

Chundong Wang,[†] Yan-Sheng Li,[‡] Jianjun Jiang,[†] and Wei-Hung Chiang*[,‡]

[†]School of Optical and Electronic Information, Huazhong University of Science and Technology, Wuhan 430074, People's Republic of China

[‡]Department of Chemical Engineering, National Taiwan University of Science and Technology, Taipei, 10607, Taiwan

Supporting Information

ABSTRACT: An effective, large-scale synthesis strategy for producing graphene nanoribbons (GNRs) with a nearly 100% yield has been proposed using a stepwise, solution-based, lengthwise unzipping carbon nanotube (CNT) method. Detailed Raman and X-ray photoelectron spectroscopy (XPS) analysis suggest that GNRs with tunable density of oxygen-containing functional groups on the GNR surfaces can be synthesized by adjusting the oxidant concentration during the CNT unzipping. The electrochemical characterization reveals that the as-produced GNRs with 42.91 atomic percent (atom %) oxygen-containing functional groups deliver a capacity of 437 mAh g^{-1} after 100 cycles at 0.33C, while the as-produced GNRs with higher oxygen-containing functional groups only present a capacity of 225 mAh g^{-1}. On the basis of the electrochemical assessment and XPS analysis, the funtionals groups (epoxy-, carbonyl-, and carboxyl groups) in GNRs could be the effective contributor for the high-performance Li-ion batteries with appropriate adjustment.

KEYWORDS: *graphene nanoribbon, unzipping, oxygen-functional groups, anode, lithium ion battery*

1. INTRODUCTION

Energy storage devices such as batteries and capacitors have been demonstrated as useful and important solutions for powering portable electronics (e.g., cellular phones, laptop computers, and cameras).[1,2]Among those energy storage devices, lithium ion batteries (LIBs) have attracted considerable attention due to their high energy density; flexible, lightweight design; and long lifespan compared with the conventional battery technologies.[3] Additionally, rechargeable LIBs also extend to large-scale applications in hybrid electric vehicles (HEVs), plug-in hybrid electric vehicles (PHEVs), and load-leveling installations on power grids.[4,5] Basically, the performance of LIBs strongly depends on the electrode materials. Graphite is the current commercial anode material due to its natural abundance, relative safety, and stable native properties compared with Si,[6] Sn,[7] and metal oxides.[8,9] The lithium ion (Li^+) is inserted into the layers of graphite instead of the happened redox reaction during the Li^+ uptake and release processes, which experiences large volume changes. However, commercialized graphite has a low theoretical capacity (372 mAh g^{-1}), which dramatically limits its further applications.[10] Consequently, the development of new nanostructured carbon materials has been highly desired to achieving high performance LIBs.

Graphene nanoribbons (GNRs), a quasi-one-dimensional form of graphene, has attracted considerable attention due to its excellent electronic stability, thermal stability, high aspect ratio, and low percolation threshold.[11] Recent theoretical and experimental works demonstrated that GNRs are promising materials for energy storage applications.[12−14] Peralta et al.[15] calculated the lithium storage capacities of GNRs, fullerenes, and graphene nanosheets (GNS) using the density functional theory and found that the storage capacity of the zigzag GNRs is 50% larger than that of GNS. It was also observed that the shape of the edge and the width influences the conductivity of the nanoribbon dramatically. Zigzag-shaped edges could be metallic, and armchair-shaped edges are semimetallic or semiconductive, which depends on the width.[16] Rangel et al. pointed out that the unzipped CNTs end up with Zigzag-shaped edges no matter what the start is by using ab initio density functional theory calculations of an unzipping process.[17] More detailed electronic behaviors of GNRs were disclosed by Kou et al. by using a first-principles study.[18,19] Furthermore, Uthaisar et al.[20] found that the lithium diffusion

Received: June 3, 2015
Accepted: July 21, 2015
Published: July 21, 2015

DOI: 10.1021/acsami.5b04864
ACS Appl. Mater. Interfaces 2015, 7, 17441−17449

coefficient of GNRs is 2 orders of magnitude higher that of GNS. It was suggested that the robust mechanical property and large surface area are two of the reasons to achieve outstanding GNRs-based LIBs in terms of durability and capacity.[21] Despiteits advantages for LIBs, the development of facile and large-scale methods for controllable production of high-quality nanoribbons is a hard task, as it tends to curve into tube structures or stack because of polarization interactions due to its intrinsic instability.[22] Kosynkin and Shimizu et al.[23,24] successfully produced GNRs in a bulk quantity using chemical oxidation by longitudinal cutting and unraveling multiwalled carbon nanotubes (MWCNTs) in concentrated sulfuric acid (H_2SO_4) and potassium permanganate ($KMnO_4$). Dai et al.[25] fabricated narrow width GNRs with 10−20 nm using argon (Ar) plasma etching of CNTs partly embedded in a polymer film, while Kato et al.[26] found GNRs can be directly converted from nickel nanobars by a rapid-heating plasma chemical vapor deposition. Moreover, other methods including metal catalyst assisted cutting,[27,28] lithium insertion and exfoliation,[29] mechanical sonication in organic solvents,[30] e-beam lithography,[31,32] and nanowire lithography[33,34]have also been proposed for production of GNRs. Among those methods, longitudinal unzipping of CNTs by chemical oxidation with suitable oxidant(s) should be one of the most effective ways in achieving low-cost and scalable synthesis of GNRs.[35] In addition, it is also possible to generate oxygen-containing groups around the GNRs using this method, making the GNRs process the solution processability for industrial-oriented electrode preparation.[36]

Herein, we describe a stepwise, solution-based oxidative process for producing a nearly 100% yield of GNRs by lengthwise unzipping the MWCNT side walls. While oxidative unzipping of MWCNTs has previously been achieved,[23,37] our unique method processes the ability to synthesis GNRs with nearly 100% yield using a very low amount of H_2SO_4 (1 mg/mL of CNT concentration in H_2SO_4). The first step, which is key, is to reduce the van der Waals forces between the coaxial graphene cylinders of MWCNTs by introducing a pretreatment of raw MWCNTs with potassium nitrate (KNO_3) and H_2SO_4, while the second step is to use $KMnO_4$ as the oxidant to unzip MWCNTs. The nitrate ions (NO_3^-) can assist sulfate ions (SO_4^{2-}) to debundle the bundled MWCNTs structure and intercalate into the coaxial graphene cylinder of CNTs, making it possible to produce GNRs with a low amount of H_2SO_4 during the CNT unzipping. The extensive scanning electron microscopy (SEM), high-resolution transmission electron microscopy (HRTEM) and X-ray diffraction (XRD) characterizations shows a nearly 100% yield of GNRs produced in our method. Systematic high-resolution X-ray photoelectron spectroscopy (HRXPS) characterization suggests that the types and concentrations of functional groups attached on the surface of as-produced GNRs are controllable by adjusting the amount of $KMnO_4$ during oxidation, giving a way to control the defect densities of the as-produced GNRs. The electrochemical performance reveals that defects allow Li^+ to migrate through the vacancies into the interlayers, providing more non-equivalent sites for Li^+ storage.

2. EXPERIMENTAL SECTION

2.1. Chemicals. Potassium permanganate ($KMnO_4$, 98%), hydrogen peroxide (H_2O_2, 35%) and ether [$(C_2H_5)_2O$, 99+%] were purchased from ACROS. Potassium nitrate (KNO_3, 95%) was obtained from JT-Baker. Sulfuric acid (H_2SO_4, > 95%) and hydrochloric acid (HCl, 37%) were purchased from Scharlau. All chemicals were used without any further purification.

2.2. CNT Synthesis. The CNTs used in the present study were synthesized using catalytic chemical vapor deposition (CVD). Details of the CNT growth process were similar to that previously described.[38] In brief, Fe films (3.0 nm thickness) and an alumina (Al_2O_3) support layer (40 nm thickness) sputtered onto 2 × 2 cm polished silicon (Si) substrates with a silicon dioxide (SiO_2) layer of 600 nm were used as the catalyst films for CNT growth. The CNTs were synthesized at 1 atm pressure in a 3 in. quartz tube furnace with two process steps, including catalyst particle formation and CNT growth. For a typical catalyst particle formation experiment, we first flowed 200 sccm (standard cubic centimeter per minute at 1 atm) helium (He) and 1800 sccm hydrogen (H_2) for 15 min while ramping the temperature from room temperature to 810 °C, then we kept the same gas flow rates for 15 min to anneal the catalyst particles. Then, CNT growth began for 10 min using a water-assisted CVD process at 810 °C with the gas mixture of 100 sccm ethylene (C_2H_4) and 900 sccm H_2, and 100 ppm water vapor as the carbon precursor and the catalyst preserver and enhancer, respectively. Water vapor of 100 ppm was supplied by passing 1000 sccm He carrier gas through a water bubbler with deionized (DI) water at STP (STP denotes standard condition for temperature and pressure, NIST version) condition. Water vapor concentration was monitored by a single-channel moisture meter (General Electric, MMS 35-211-1-100) coupled with a moisture probe (General Electric, M2LR) installed before the CVD reactor. All gas flows were controlled by mass flow controllers that were carefully calibrated before experiments to precisely control the gas concentrations in the CVD reactor.

2.3. Preparation of GNRs. In a typical preparation, 0.1 g of MWCNTs was suspended in 10 mL of concentrated sulfuric acid and 1g KNO_3 and then stirred at 300 rpm for 2 h using a magnetic stirrer until a visually homogeneous black solution formed. Then, $KMnO_4$ with different amounts was slowly added to the solution and further stirred for 2 h at room temperature. After that, the temperature was gradually raised to 70 °C and maintained at that temperature for 2 h in a water bath (IKA-HS7 digital). Detailed reaction conductions are summarized in Table 1. When the reaction was complete, the product

Table 1. Summarized Reaction Conditions of Chemical Oxidation of MWCNT Unzipping

sample	$KMnO_4$ (g)
0.375	0.375
0.5	0.500
0.75	0.750

was purified and dried with a series steps reported elsewhere. Briefly, each mixture was removed from the heat source, cooled to room temperature, and poured into 350 g of ice containing 5 mL of 35% H_2O_2 (to prevent precipitation of insoluble MnO_2). The mixtures were then centrifuged (24 500 rpm, 30 min) to give crude GNRs solid. The solid was removed and then bath-sonicated in DI water 60 mL for 30 min. The material was then bath sonicated again by adding 30 mL HCl, the product was centrifuged (24 500 rpm, 30 min). In the end, the collected solid was then dispersed in ether (60 mL) for 30 min and then centrifuged (24 500 rpm, 30 min). The purified GNRs were collected. The detailed preparation process is schematically depicted in Figure 1.

2.4. Characterization. The scanning electron microscopy (SEM) images of as-produced samples were recorded on JEOL JSM-6500F (accelerating voltage = 15 kV). Samples were prepared by pressing powders on the copper tape. The transmission electron microscopy (TEM) images of MWCNTs and as-produced GNRs were collected on HITACHI H-9500. Samples were prepared by dispersion in ethanol and then dropped onto 300 mesh holey lacy carbon grids on cupper support (Ted Pella, Inc.). X-ray photoemission spectroscopy (XPS) was carried out on VG ESCA Scientific Theta Probe with a pass energy of 50 eV, 53° take off angle, and a 400 μm beam size. Samples

DOI: 10.1021/acsami.5b04864
ACS Appl. Mater. Interfaces 2015, 7, 17441−17449

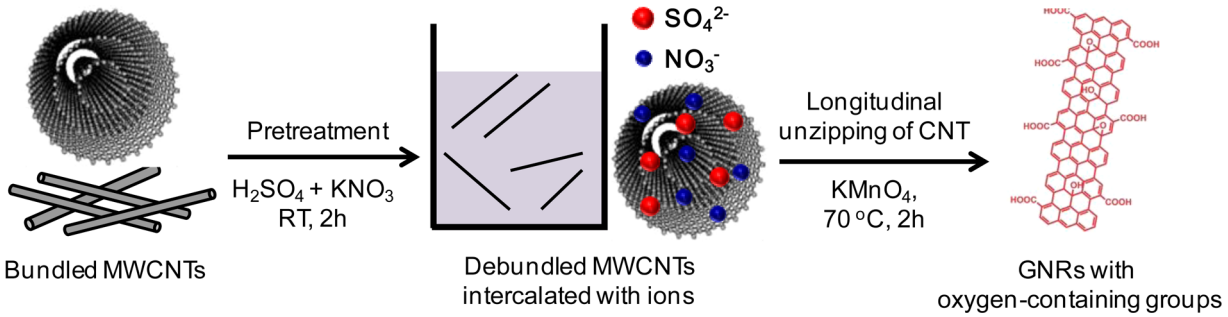

Figure 1. Schematic illustration of the stepwise, solution-based oxidative process for producing GNRs by longitudinal unzipping the MWCNT side walls.

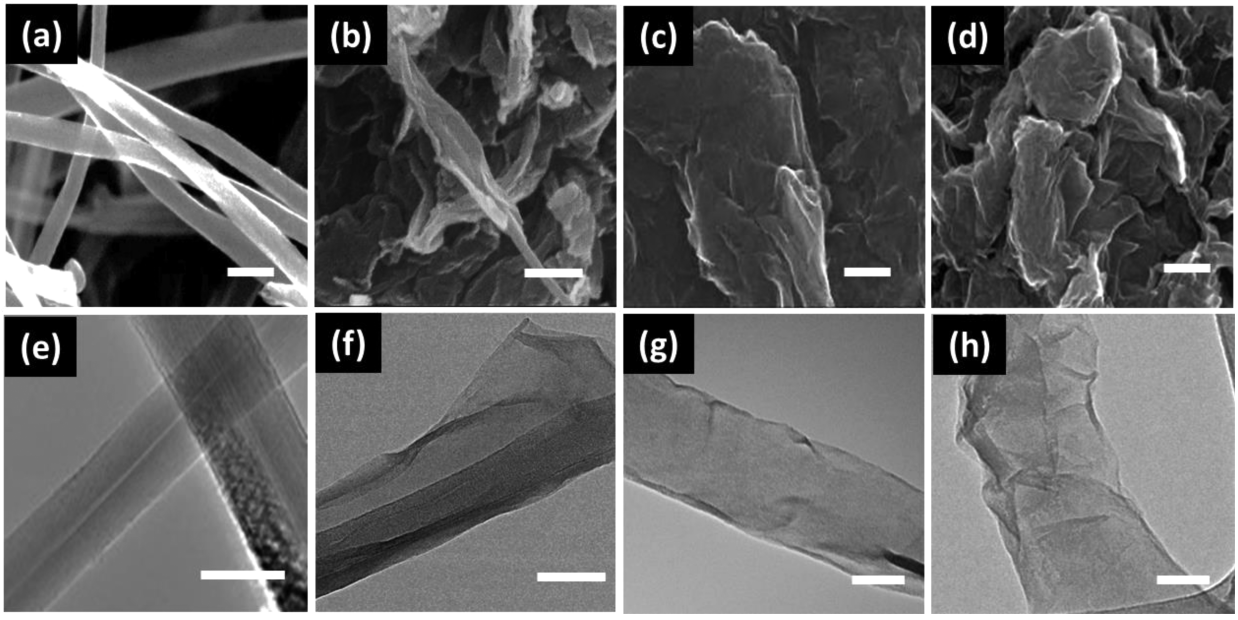

Figure 2. SEM images of (a) pristine MWCNTs, (b) sample 0.375, (c) sample 0.5, and (d) sample 0.75; TEM image of (e) pristine MWCNTs, (f) sample 0.375, (g) sample 0.5, and (h) sample 0.75. All scale bars = 50 nm.

were dispersed in ethanol and formed thin film on silicon substrates. The powder X-ray diffraction (XRD) were obtain by BRUKER D2 PHASER X-ray Powder Diffraction (Cu Kα, λ= 1.54 Å). The Raman spectra of pristine CNTs and as-pretreated samples were performed on JASCO NRS-5100 at 532 nm excitation. The FTIR spectra of pristine CNTs and as-prepared samples were collected on Biorad FTS 3500.

2.5. Electrochemical Measurements. Electrochemical measurements of the GNRs were carried out with LIR2032 Coin-type half-cells assembled in an argon-filled glovebox (MB200MOD). Then, 1.0 mol/L of $LiPF_6$ solution, a mixture of ethylene carbonate (EC)/dimethylcarbonate (DMC)/diethylcarbonate (DEC) (1:1:1, vol/vol/vol) was applied as the electrolyte. A Celgard 2400 microporous polypropylene membrane was usedas the separator and Li foil was utilized as the counter electrode. The CV measurement was collected on an Electrochemical Workstation (Model 600D series) at a scan rate of 0.1 mV/s vs Li/Li^+ at room temperature. Cycling performances under 0.33 C were tested with the first cycle at 0.1 C and then two cycles at 0.2 C at the beginning.

3. RESULTS AND DISCUSSION

Figure 2a shows a typical SEM image of MWCNTs, which are used as the raw materials for synthesis of GNRs. It can be seen that the MWCNT is 40−50 nm in diameter and at least several hundred nanometers in length. Figure 2b− d demonstrates the SEM images of samples 0.375, 0.5, and 0.75. An unzipped MWCNT of sample 0.5 and 0.375 was captured, as demonstrated in Figure 2b, verifying our oxidation method of MWCNT unzipping is successful. Different from the observed curved edge of GNR in local part in Figure 2b, samples 0.5 and 0.75 were aggregated together, as displayed in Figure 2c,d, from which the ribbon structures cannot be very easily distinguished. The reason could be assigned to the drying process for SEM observation. To see the morphology of the GNRs of the different samples more clearly, we recorded TEM images, as depicted in Figure 2(f−h). For comparison, the TEM image of MWCNTS were also recorded as displayed in Figure 2e, from which the hollow characteristic of a tube can be well observed. Consistent with the observation in Figure 2b, the graphene ribbon of sample 0.375 in the TEM image was also curved. In sample 0.5 (Figure 2g), a regular thin layer of GNR with some folds on the surface was revealed due to the well dispersion. Unfortunately, we still have no ability to directly identify the edge structure to be zigzag- or armchair-shape by TEM observation, due, in part, to the edge curling and the extensive edge oxidation, which could be removed only by heating over 2000 °C, which will lead to reconstruction and modified electronic properties.[23] The TEM results indicate that the synthesized GNRs have high aspect ratios as well as edge effect. Figure2h shows the strip-type graphene ribbon of sample 0.75,

DOI: 10.1021/acsami.5b04864
ACS Appl. Mater. Interfaces 2015, 7, 17441−17449

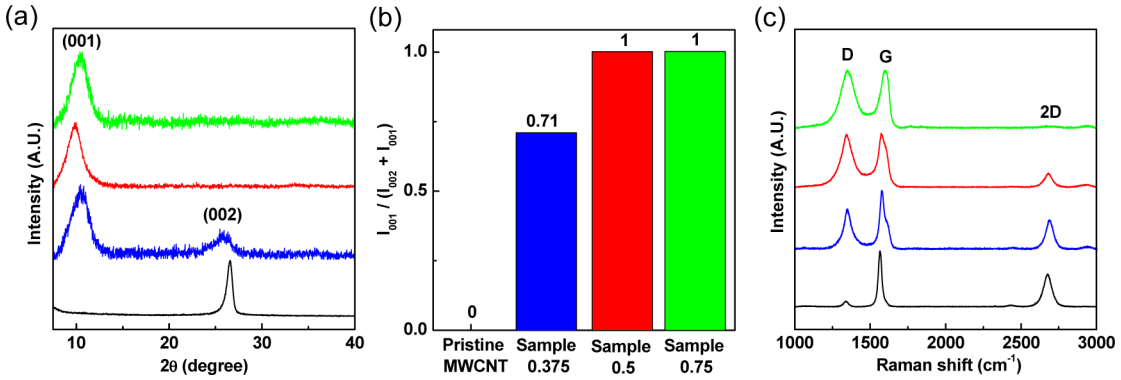

Figure 3. (a) XRD patterns of (black) pristine MWCNTs, (blue) sample 0.375, (red) sample 0.5, and (magenta) sample 0.75. (b) Relative peak intensity ratios ($I_{001}/(I_{002} + I_{001})$) of MWCNTs and the tree samples. (c) Raman spectra of MWCNTs and the three samples.

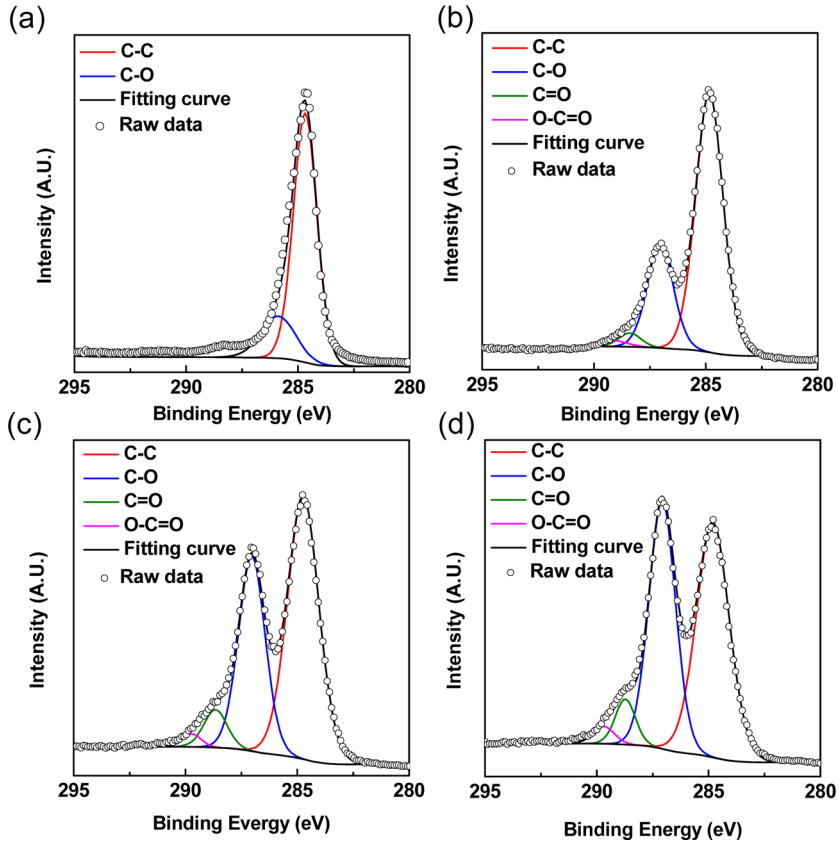

Figure 4. HRXPS C 1s spectra of (a) pristine MWCNTs, (b) sample 0.375, (c) sample 0.5, and (d) sample 0.75.

which is quite similar to the one of sample 0.5. The difference can be easily distinguished. The morphology of sample 0.75 tends to be irregular with many wrinkles in the surface and the edge, which may be due to the over oxidation during the synthesis process.

Figure3a shows the typical X-ray diffraction (XRD) patterns of the as-prepared GNRs (i.e., samples 0.375, 0.5, and 0.75). For comparison, the XRD pattern of MWCNT was also collected, and a strong peak at 26.3° was observed, which should be assigned to (002) diffraction of the graphitic layer-by-layer structure with interlayer spacing of 0.34 nm.[13,39] After treating with the strong oxidant (sample 0.375), the intensity of the peak in 26.3° decreased, while a strong as well as broad peak located at ~11° appeared, suggesting that the CNT has been well oxidized. In other words, the CNTs were successfully unzipped. With a further increase in the amount of $KMnO_4$ during the oxidation treatment process of samples 0.5 and 0.75, the peak at 26.3° disappeared. The reason can be attributed to the further oxidization of GNRs, which means that oxygen-containing functional groups were attached on the graphene ribbon sheets, which results in a lattice space increase in the (002) phase.[9,40] Nonetheless, no obvious difference of the XRD patterns of samples 0.5 and 0.75 can be seen, which may need to refer to other characterization technologies. The production yield of GNRs can be quantitative estimated from the ratio of the peak intensity of oxidized GNR (I_{001}) to the summation of peak intensities of CNT (I_{002}) and GNR (I_{001}) in the XRD patterns,[41] as shown in Figure 3b. The quantitative yield of samples 0.5 and 0.75 is 100%, and the yield of sample 0.375 is 0.71, suggesting that sample 0.375 is completely oxidized in the

DOI: 10.1021/acsami.5b04864
ACS Appl. Mater. Interfaces 2015, 7, 17441−17449

unzipping process. We should point out that, compared with other reported chemical oxidation approaches,[23,24] our unzipping approach used a low dose of H_2SO_4 (10 mg/mL of CNT concentration in H_2SO_4), which is only 10% of that used by Kosynkin et al.[23] The key factor for the success of our method the pretreatment of raw CNTs with KNO_3 under the reported condition, which allows K^+ and NO_3^- to assist SO_4^{2-} in exfoliating the bundled CNTs and intercalate into the coaxial graphene cylinders of CNTs. In the second step, it tuned the surface functionalities of the as-produced GNRs by controlling the concentrations of $KMnO_4$ as the oxidant to unzip MWCNTs under suitable conditions (oxidant concentration, temperature, and time). With such a stepwise treatment, it is possible to significantly reduce the van der Waals attractions between individual tubes and the coaxial graphene cylinders of CNTs with a very low amount of H_2SO_4. Because it reduces the usage of strong acid, we proposed that our environmentally friendly approach is suitable for an industrial-scale production.

The Raman spectra of pristine MWCNTs and GNRs were revealed in Figure 3c. It can be seen that the pristine MWCNTs feature three peaks at 1337.1, 1564.8, and 2673.2 cm^{-1}, which are assigned to the D band, G band, and 2D band of carbon, respectively. The D band at 1337.1 cm^{-1} originates from a second-order Raman scattering process, involving one iTO phonon and one defect near the K point.[42] The G band at 1564.8 cm^{-1} is the so-called characteristic peak of graphite, which corresponds to the doubly degenerate E_{2g} symmetry phonon mode (iTO and LO) of graphite at the Brillouin zone center and results from the emission of zone-center optical phonons.[42−44] The 2D band centered at 2673.2 cm^{-1} is generated by two iTO phonons with opposite momentum in the highest optical branch near the K and can be well fitted by a single Lorentzian function.[45,46] After the strong oxidant treated (sample 0.375), the intensity of D band increased obviously, which informs us that defects or edge effects was introduced into the GNRs. The defects could be holes with different shapes and sizes on the basal plane of the ribbon, which was caused by the initial manganate ester formation and the further cleavage of C−C bonding introduced by the vicinal diols.[47] Meanwhile, the attached oxygen functional groups (i.e., epoxy groups, carbonyl, and carboxyl groups) at the edges and surface were also regarded as the defects.[47] This observation is consistent with the XRD results, which are given in Figure 3a. When $KMnO_4$ was increased to 0.5 g in the oxidation reaction (sample 0.5), the intensity of D band was further increased, while the intensity of 2D band decreased, verifying that more functional groups were attached to the GNRs. However, when the amount of $KMnO_4$ was further increased to 0.75 (sample 0.75), 2D band disappeared accompanied by more strong D band showing, suggesting that too many defects were introduced into graphene nanoribbon lattice in this case, and the GNRs tend to be amorphous.

To further study the chemical bonding state of GNRs with different oxidation, we carried out HRXPS characterization on the three different samples and MWCNTs. Figure 4a exhibits C 1s spectra of the pristine MWCNT, of which two peaks centered at 284.6 and 285.9 eV were seen, which are attributed to graphite-like sp^2-C and epoxy groups. When the oxidization treatment was carried out (sample 0.375) as shown in Figure 4b, an obvious peak appeared in the left of the main peak. After carefully deconvolution and fitting, it can be split into four peaks, namely graphite-like sp^2-C (C−C) at 284.8 eV, epoxy groups (C−O) at 287.0 eV, carbonyl groups (C═O) at 288.4 eV, and carboxyl groups (COOH) at 288.9 eV.[47]The XPS quantification result is summarized in Table 2. This observation

Table 2. Atomic Percentages of Different Carbon Bonds Identified by XPS in Pristine CNTs and Different As-Produced GNR Samples

sample	C−C (atom %)	C−O (atom %)	C═O (atom %)	COOH (atom %)
pristine CNTs	89.97	13.03	0	0
sample 0.375	69.06	26.31	2.94	1.69
sample 0.5	57.09	35.84	6.26	1.61
sample 0.75	49.59	42.17	5.87	2.37

is consistent with the result of FTIR shown in Figure S1 (Supporting Information). Compared with the pristine CNTs, strong peaks at 1647 cm^{-1}(purple region) and 3445 cm^{-1} (light green region) in sample 0.375 appeared, which assigns to a C═O and COO−H/O−H stretch, of which it further verifies that numerous carboxyl and hydroxyl functionalities were attached on the graphene nanoribbons. Bhardwaj et al.[48] proposed that the oxygen atoms attached to the tube walls would distort neighboring alkenes, which makes them more easily to be oxidized and opened. Thus, we can conclude that the unzipping of carbon nanotubes is due to the attached epoxy, carbonyl, and carboxyl groups on the defective sites and edges of GNRS. When more $KMnO_4$ was added into the reaction (sample 0.5), as shown in Figure 4c, the peak intensities of attached functional groups (i.e., epoxy, carbonyl, and carboxyl groups) were all increased. Note that in sample 0.375 and sample 0.5, the intensity of graphite-like sp^2-C is still the strongest (taken over 69.06 atom % and 57.09 atom %), though the epoxy group is even quite close to it in sample 0.5, suggesting that it still maintain the sp^2 C−C structure in sample 0.375 and sample 0.5. When $KMnO_4$ was further increased (sample 0.75), the intensities of epoxy groups, carboxyl groups, and carbonyl groups all increased. Nonetheless, it is well noticed that the peak intensity of carbonyl groups is even larger than that of sp^2-C in this case, which indicates that a large number of defects were introduced into GNRs. In this case, the sum of oxygen-containing functional groups accounted for 50.41 atom % in the GNRs' lattice. We propose that the GNRs tend to be amorphous, which is consistent with the observation in Raman spectra as well as XRD. On the basis of the above material characterizations, it is suggested that controllable synthesis of GNRs with tunable surface functionalities can be achieved using our method.

To reveal the role of the attached oxygen-functional groups in GNRs, the electrochemical behavior of fresh sample 0.375, sample 0.5, and sample 0.75 at the first three cycles were evaluated with cyclic voltammograms (CVs) as shown in Figure 5. All curves displayed the typical CV curves of carbonaceous anode materials at the first cathodic scan. In sample 0.375, the observed peak at ∼0.58 V in the first cycle should be attributed to the irreversible formation of solid electrolyte interface (SEI) films due to the decomposition of electrolytes[49] and the reaction of lithium ions with residual acid,[50] which is the reason for the initial irreversible capacity. This peak disappeared in the second and third cycles, suggesting that the surface of the passivated GNRs have been stable. When more oxygen-functional groups were introduced into the GNRs (sample 0.5), another peak at ∼1.24 V appeared accompanied by the peak at ∼0.58 V in the first cycle (shown in Figure 5b),

DOI: 10.1021/acsami.5b04864
ACS Appl. Mater. Interfaces 2015, 7, 17441−17449

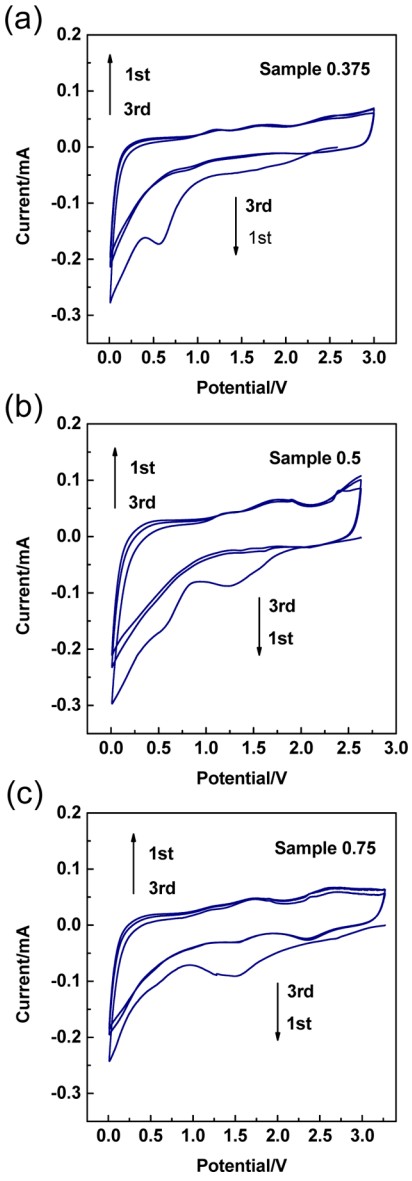

Figure 5. Cyclic voltammograms (CVs) of the first three cycles at a scan rate of 0.1 mV s^{-1} for (a) sample 0.375, (b) sample 0.5, and (c) sample 0.75.

indicating some defects have been created on the nanoribbons. This allows more Li^+ extraction from the two sides of nanoribbon in comparison with one side extraction from CNT. This observation is consistent with the reported results of balled milled CNTs[51] and chemically etched CNTs.[52] Thus, it presents evidence that surface defects, here is the attached functional group, providing more sites for lithium storage. With further increasing the attached oxygen-functional groups, the peak at 0.58 V has been totally disappeared in the first cycle. Instead, a new peak at 2.37 V is seen, which is due to the adsorption of the Li^+ on the remaining functional groups, of which it consistent with the XPS results that too much defects were introduced into the graphene nanoribbon sheets. It means that over oxidation results in the totally destroy of the graphene lattice structure, of which the conductivity as well as the lithium storage capacity will be dramatically influenced.

Figure 6a–c shows the charge–discharge profiles of GNRs in the first three cycles at a current density of 0.33C (1C = 372 mAh g^{-1}) ranging from 0 to 3 V. The initial discharge capacities of sample 0.375, 0.5, and 0.75 were 1188, 1338, and 1335 mAh g^{-1}, respectively, while the charge capacities of them were 577, 628, and 495 mAh g^{-1}, respectively, corresponding to initial Coulombic efficiencies of 48.6, 46.9, and 37%. The irreversible capacity loss in the first cycle should be attributed to the formation of the SEI layer, mentioned previously. It is worth noting that Coulombic efficiency decreases dramatically with the amount of attached functional group increase, indicating that the adsorption of Li^+ on functional groups have a big contribution to the irreversible capacity. Another reason for the low Coulombic efficiency is that the high surface areas of GNRs provide a large contact area between electrode and electrolyte to form SEI layer by consuming large amount of Li^+. It is worth noting that the initial discharge capacity is much higher than that of commercial carbon,[53] suggesting that the lithium storage mechanism of GNRs is different from the conventional graphite interaction approach. The difference is also reflected in the charge–discharge profile. Different from the long plateau after 0.5 V versus Li^+/Li in graphite,[54] the slope starts at about 2.5 V in GNRs. All our GNRs deliver high specific capacities below 0.5 V without obvious plateau, providing evidence that at least two different Li^+ storage mechanisms exist. It is well-known that in the sp^2 hybrid graphite, it refers to lithium ion intercalation and deintercalation during the charging and discharging process, of which it forms LiC_6 compounds. Herein, the gradual decline tendency in discharging process is similar the Li^+ storage behavior observed in graphene[55] and hard carbon.[54] We propose that the obtained capacity comes from the following two parts: (1) The capacity in the lower voltage (<0.5 V), which contributes from the lithium intercalation in the GNRs. Due to the absence of a potential plateau, especially in samples 0.5 and 0.75, it suggests that the disordered stacked graphene nanosheet structures result in electrochemically and geometrically nonequivalent Li^+ sites. (2) The capacity above 0.5 V is assigned to a faradic capacitance either on the GNRs surface or on the edge plane.[55]

The cycle performances of GNRs at a current density of 0.33C are demonstrated in Figure 6d. The three samples exhibit the same tendency, which keep decreasing in the first several cycles and then being stable in the following cycles. Compared with sample 0.375 and 0.75, sample 0.5 has the highest specific capacity of 437 mAh g^{-1} among the three samples after 100 cycles, while samples 0.375 and 0.75 have capacities of 392 and 225 mAh g^{-1}, respectively. Combined with XPS analysis, it can be found that the capacity was increased with adding more oxygen-functional groups on GNRs. However, when the GNRs were over oxidized, the capacity decreases dramatically from 437 to 225 mAh g^{-1}. Thus, we propose that the oxygen-functional groups may contribute to the increased capacity as it provides more nonequivalent sites for Li^+ storage. We should also emphasis that sample 0.75 tends to be disordered, as the 2D band totally disappeared in the Raman spectrum with increasing the amount of the attached oxygen-functional groups. This observation could be good evidence to indicate that too many defects introduced into the graphene sheets will degrade the crystallinity as well as the Li^+ storage capability of GNRs, of which the similar performance was also seen by Xiao et al.[14]

To further examine the different rate capability of the three samples, we carried out the galvanostatic charge–discharge measurements at various current densities, which range from 0.1 to 2C (Figure 6e). Outstanding rate capability is revealed in

DOI: 10.1021/acsami.5b04864
ACS Appl. Mater. Interfaces 2015, 7, 17441–17449

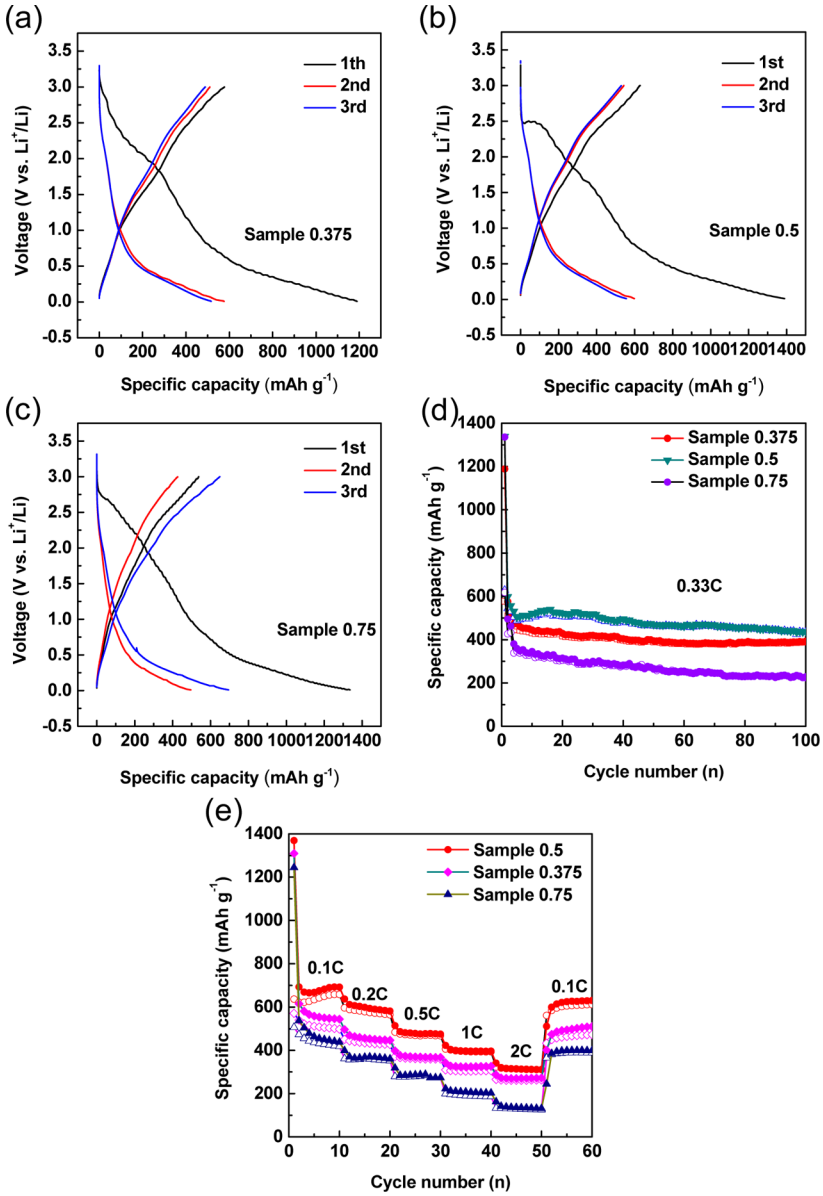

Figure 6. Charge−discharge profiles of the first, second, and third cycles of (a) sample 0.375, (b) sample 0.5, and (c) sample 0.75. (d) Cycling performance of samples 0.375, 0.5, and 0.75 between 0.0 and 3.0 V vs Li/Li^+ at a current density of 0.33C. (e) Rate performance of samples 0.375, 0.5, and 0.75; (solid symbols) discharge and (open symbols) charge.

sample 0.5. It exhibits 689, 590, 480, 396, and 312 mAh g^{-1} at 0.1, 0.2, 0.5, 1, and 2C. Note that the effect of the attached functional group in improving the faradic capacitance on the surface or edge sites of GNRs will be especially obvious at high current densities.[56] When the current density was restored to 0.1C after 50 cycles, the capacity of 629 mAh g^{-1} could still be successfully achieved and kept stable. This performance is comparable or even superior to other reported GNRs.[13,12,14] Moreover, in Figure 6d, it can be seen that sample 0.75 presents the lowest delivered capacity, while sample 0.375 depicts a little bit lower capacity than that of sample 0.5. The difference between the three samples is consistent with the cycling performances described in Figure 6d.

4. CONCLUSIONS

In summary, we have developed a facile and large-scale approach for controllable synthesis of GNRs with nearly100% yield and tunable surface functionalities using a solution-based lengthwise unzipping the MWCNT side walls. With the analysis of XRD, Raman, XPS, it found that the defects (attached functional groups) in the GNRs lattice can be tuned, which results in different delivered specific capacities under the same test condition. The middle oxidized one (sample 0.5) delivers a capacity of 437 mAh g^{-1} at 0.33C, while low oxidized one (sample 0.375) and high oxidized one (sample 0.75) present capacities of 392 mAh g^{-1} and 225 mAh g^{-1}, respectively. Defects created during the oxidation treatment process allow Li^+ migrate through the vacancies into the interlayers, providing more sites for the accommodation of Li^+. Additionally, we also proved that too much introduced oxygen-functional groups will degrade the crystallinity of graphene nanoribbon sheets, which will dramatically decrease the Li^+ storage capacity. Thus, our study on the lithium ion battery performance of GNRS provides a strong reference for future application of carbon material and its composites by adjusting the amount of functional groups.

DOI: 10.1021/acsami.5b04864
ACS Appl. Mater. Interfaces 2015, 7, 17441−17449

■ ASSOCIATED CONTENT

Supporting Information

The Supporting Information is available free of charge on the ACS Publications website at DOI: 10.1021/acsami.5b04864.

FT-IR spectra of pristine MWCNTs and as-synthesized GNRs (PDF)

■ AUTHOR INFORMATION

Corresponding Author

*E-mail: whchiang@mail.ntust.edu.tw.

Notes

The authors declare no competing financial interest.

■ ACKNOWLEDGMENTS

This work was supported by National Natural Science Foundation of China (NSFC, Grant nos. 51408085 and 51402344), the Ministry of Science and Technology of Taiwan (MOST, Grant no. NSC 102-2218-E-011-022-MY2), and the National Taiwan University of Science and Technology (NTUST). C.D.W. acknowledges the start research foundation of Huazhong University of Science and Technology.

■ REFERENCES

(1) Tarascon, J.-M.; Armand, M. Issues and challenges facing rechargeable lithium batteries. *Nature* **2001**, *414*, 359−367.

(2) Li, H.; Wang, Z.; Chen, L.; Huang, X. Research on Advanced Materials for Li-ion Batteries. *Adv. Mater.* **2009**, *21*, 4593−4607.

(3) Sun, X.; Yan, C.; Chen, Y.; Si, W.; Deng, J.; Oswald, S.; Liu, L.; Schmidt, O. G. Three-Dimensionally "Curved" NiO Nanomembranes as Ultrahigh Rate Capability Anodes for Li-Ion Batteries with Long Cycle Lifetimes. *Adv. Energy Mater.* **2014**, *4*, 1300912.

(4) Lou, X. W.; Deng, D.; Lee, J. Y.; Feng, J.; Archer, L. A. Self-Supported Formation of Needlelike Co3O4 Nanotubes and Their Application as Lithium-Ion Battery Electrodes. *Adv. Mater.* **2008**, *20*, 258−262.

(5) Xu, Y.; Yi, R.; Yuan, B.; Wu, X.; Dunwell, M.; Lin, Q.; Fei, L.; Deng, S.; Andersen, P.; Wang, D. High capacity MoO2/graphite oxide composite anode for lithium-ion batteries. *J. Phys. Chem. Lett.* **2012**, *3*, 309−314.

(6) Wang, C.; Chui, Y.-S.; Ma, R.; Wong, T.; Ren, J.-G.; Wu, Q.-H.; Chen, X.; Zhang, W. A three-dimensional graphene scaffold supported thin film silicon anode for lithium-ion batteries. *J. Mater. Chem. A* **2013**, *1*, 10092−10098.

(7) Wang, C.; Li, Y.; Chui, Y.-S.; Wu, Q.-H.; Chen, X.; Zhang, W. Three-dimensional Sn−graphene anode for high-performance lithium-ion batteries. *Nanoscale* **2013**, *5*, 10599−10604.

(8) Xu, S.; Hessel, C. M.; Ren, H.; Yu, R.; Jin, Q.; Yang, M.; Zhao, H.; Wang, D. α-Fe 2 O 3 multi-shelled hollow microspheres for lithium ion battery anodes with superior capacity and charge retention. *Energy Environ. Sci.* **2014**, *7*, 632−637.

(9) Wang, C.; Zhang, Q.; Wu, Q.-H.; Ng, T.-W.; Wong, T.; Ren, J.; Shi, Z.; Lee, C.-S.; Lee, S.-T.; Zhang, W. Facile synthesis of laminate-structured graphene sheet−Fe 3 O 4 nanocomposites with superior high reversible specific capacity and cyclic stability for lithium-ion batteries. *RSC Adv.* **2012**, *2*, 10680−10688.

(10) Landi, B. J.; Ganter, M. J.; Cress, C. D.; DiLeo, R. A.; Raffaelle, R. P. Carbon nanotubes for lithium ion batteries. *Energy Environ. Sci.* **2009**, *2*, 638−654.

(11) Son, Y.-W.; Cohen, M. L.; Louie, S. G. Half-metallic graphene nanoribbons. *Nature* **2006**, *444*, 347−349.

(12) Liu, Y.; Wang, X.; Dong, Y.; Wang, Z.; Zhao, Z.; Qiu, J. Nitrogen-doped graphene nanoribbons for high-performance lithium ion batteries. *J. Mater. Chem. A* **2014**, *2*, 16832−16835.

(13) Mei, T.; Zhang, L.; Wang, X.; Qian, Y. One-pot synthesis of carbon nanoribbons and their enhanced lithium storage performance. *J. Mater. Chem. A* **2014**, *2*, 11974−11979.

(14) Xiao, B.; Li, X.; Li, X.; Wang, B.; Langford, C.; Li, R.; Sun, X. Graphene nanoribbons Derived from the unzipping of carbon nanotubes: Controlled synthesis and superior lithium storage performance. *J. Phys. Chem. C* **2014**, *118*, 881−890.

(15) Uthaisar, C.; Barone, V.; Peralta, J. E. Lithium adsorption on zigzag graphene nanoribbons. *J. Appl. Phys.* **2009**, *106*, 113715.

(16) Yang, L.; Park, C.-H.; Son, Y.-W.; Cohen, M. L.; Louie, S. G. Quasiparticle energies and band gaps in graphene nanoribbons. *Phys. Rev. Lett.* **2007**, *99*, 186801.

(17) Rangel, N. L.; Sotelo, J. C.; Seminario, J. M. Mechanism of carbon nanotubes unzipping into graphene ribbons. *J. Chem. Phys.* **2009**, *131*, 031105.

(18) Kou, L.; Tang, C.; Chen, C.; Guo, W. Hybrid W-shaped graphene nanoribbons: Distinct electronic and transport properties. *J. Appl. Phys.* **2011**, *110*, 124312.

(19) Kou, L.; Tang, C.; Frauenheim, T.; Chen, C. Intrinsic Charge Separation and Tunable Electronic Band Gap of Armchair Graphene Nanoribbons Encapsulated in a Double-Walled Carbon Nanotube. *J. Phys. Chem. Lett.* **2013**, *4*, 1328−1333.

(20) Uthaisar, C.; Barone, V. Edge effects on the characteristics of Li diffusion in graphene. *Nano Lett.* **2010**, *10*, 2838−2842.

(21) Liu, X. H.; Wang, J. W.; Liu, Y.; Zheng, H.; Kushima, A.; Huang, S.; Zhu, T.; Mao, S. X.; Li, J.; Zhang, S. In situ transmission electron microscopy of electrochemical lithiation, delithiation and deformation of individual graphene nanoribbons. *Carbon* **2012**, *50*, 3836−3844.

(22) Schmidt, O. G.; Eberl, K. Nanotechnology: Thin solid films roll up into nanotubes. *Nature* **2001**, *410*, 168−168.

(23) Kosynkin, D. V.; Higginbotham, A. L.; Sinitskii, A.; Lomeda, J. R.; Dimiev, A.; Price, B. K.; Tour, J. M. Longitudinal unzipping of carbon nanotubes to form graphene nanoribbons. *Nature* **2009**, *458*, 872−876.

(24) Shimizu, T.; Haruyama, J.; Marcano, D.; Kosinkin, D.; Tour, J.; Hirose, K.; Suenaga, K. Large intrinsic energy bandgaps in annealed nanotube-derived graphene nanoribbons. *Nat. Nanotechnol.* **2011**, *6*, 45−50.

(25) Jiao, L.; Zhang, L.; Wang, X.; Diankov, G.; Dai, H. Narrow graphene nanoribbons from carbon nanotubes. *Nature* **2009**, *458*, 877−880.

(26) Kato, T.; Hatakeyama, R. Site-and alignment-controlled growth of graphene nanoribbons from nickel nanobars. *Nat. Nanotechnol.* **2012**, *7*, 651−656.

(27) Elías, A. L.; Botello-Méndez, A. R.; Meneses-Rodríguez, D.; Jehová González, V.; Ramírez-González, D.; Ci, L.; Munoz-Sandoval, E.; Ajayan, P. M.; Terrones, H.; Terrones, M. Longitudinal cutting of pure and doped carbon nanotubes to form graphitic nanoribbons using metal clusters as nanoscalpels. *Nano Lett.* **2010**, *10*, 366−372.

(28) Parashar, U. K.; Bhandari, S.; Srivastava, R. K.; Jariwala, D.; Srivastava, A. Single step synthesis of graphene nanoribbons by catalyst particle size dependent cutting of multiwalled carbon nanotubes. *Nanoscale* **2011**, *3*, 3876−3882.

(29) Cano-Márquez, A. G.; Rodríguez-Macías, F. J.; Campos-Delgado, J.; Espinosa-González, C. G.; Tristán-López, F.; Ramírez-González, D.; Cullen, D. A.; Smith, D. J.; Terrones, M.; Vega-Cantú, Y. I. Ex-MWNTs: graphene sheets and ribbons produced by lithium intercalation and exfoliation of carbon nanotubes. *Nano Lett.* **2009**, *9*, 1527−1533.

(30) Jiao, L.; Wang, X.; Diankov, G.; Wang, H.; Dai, H. Facile synthesis of high-quality graphene nanoribbons. *Nat. Nanotechnol.* **2010**, *5*, 321−325.

(31) Han, M. Y.; Özyilmaz, B.; Zhang, Y.; Kim, P. Energy band-gap engineering of graphene nanoribbons. *Phys. Rev. Lett.* **2007**, *98*, 206805.

(32) Wang, X.; Dai, H. Etching and narrowing of graphene from the edges. *Nat. Chem.* **2010**, *2*, 661−665.

(33) Sinitskii, A.; Tour, J. M. Patterning graphene nanoribbons using copper oxide nanowires. *Appl. Phys. Lett.* **2012**, *100*, 103106.

DOI: 10.1021/acsami.5b04864
ACS Appl. Mater. Interfaces 2015, 7, 17441−17449

(34) Bai, J.; Duan, X.; Huang, Y. Rational fabrication of graphene nanoribbons using a nanowire etch mask. *Nano Lett.* **2009**, *9*, 2083−2087.
(35) Ma, L.; Wang, J.; Ding, F. Recent progress and challenges in graphene nanoribbon synthesis. *ChemPhysChem* **2013**, *14*, 47−54.
(36) Liu, J.; Kim, G. H.; Xue, Y.; Kim, J. Y.; Baek, J. B.; Durstock, M.; Dai, L. Graphene Oxide Nanoribbon as Hole Extraction Layer to Enhance Efficiency and Stability of Polymer Solar Cells. *Adv. Mater.* **2014**, *26*, 786−790.
(37) Shinde, D. B.; Majumder, M.; Pillai, V. K. Counter-ion dependent, longitudinal unzipping of multi-walled carbon nanotubes to highly conductive and transparent graphene nanoribbons. *Sci. Rep.* **2014**, *4*, 4363.
(38) Chiang, W.-H.; Futaba, D. N.; Yumura, M.; Hata, K. Growth control of single-walled, double-walled, and triple-walled carbon nanotube forests by a priori electrical resistance measurement of catalyst films. *Carbon* **2011**, *49*, 4368−4375.
(39) Zhang, K.; Zhang, Y.; Wang, S. Enhancing thermoelectric properties of organic composites through hierarchical nanostructures. *Sci. Rep.* **2013**, *3*, 3448.
(40) Zhang, K.; Zhang, L. L.; Zhao, X.; Wu, J. Graphene/polyaniline nanofiber composites as supercapacitor electrodes. *Chem. Mater.* **2010**, *22*, 1392−1401.
(41) Kovtyukhova, N. I.; Wang, Y.; Berkdemir, A.; Cruz-Silva, R.; Terrones, M.; Crespi, V. H.; Mallouk, T. E. Non-oxidative intercalation and exfoliation of graphite by Brønsted acids. *Nat. Chem.* **2014**, *6*, 957−963.
(42) Malard, L.; Pimenta, M.; Dresselhaus, G.; Dresselhaus, M. Raman spectroscopy in graphene. *Phys. Rep.* **2009**, *473*, 51−87.
(43) Wang, C.; Zhou, Y.; He, L.; Ng, T.-W.; Hong, G.; Wu, Q.-H.; Gao, F.; Lee, C.-S.; Zhang, W. In situ nitrogen-doped graphene grown from polydimethylsiloxane by plasma enhanced chemical vapor deposition. *Nanoscale* **2013**, *5*, 600−605.
(44) Qian, W.; Cui, X.; Hao, R.; Hou, Y.; Zhang, Z. Facile preparation of nitrogen-doped few-layer graphene via supercritical reaction. *ACS Appl. Mater. Interfaces* **2011**, *3*, 2259−2264.
(45) Ferrari, A.; Meyer, J.; Scardaci, V.; Casiraghi, C.; Lazzeri, M.; Mauri, F.; Piscanec, S.; Jiang, D.; Novoselov, K.; Roth, S. Raman spectrum of graphene and graphene layers. *Phys. Rev. Lett.* **2006**, *97*, 187401.
(46) Graf, D.; Molitor, F.; Ensslin, K.; Stampfer, C.; Jungen, A.; Hierold, C.; Wirtz, L. Spatially resolved Raman spectroscopy of single- and few-layer graphene. *Nano Lett.* **2007**, *7*, 238−242.
(47) Higginbotham, A. L.; Kosynkin, D. V.; Sinitskii, A.; Sun, Z.; Tour, J. M. Lower-defect graphene oxide nanoribbons from multi-walled carbon nanotubes. *ACS Nano* **2010**, *4*, 2059−2069.
(48) Bhardwaj, T.; Antic, A.; Pavan, B.; Barone, V.; Fahlman, B. D. Enhanced electrochemical lithium storage by graphene nanoribbons. *J. Am. Chem. Soc.* **2010**, *132*, 12556−12558.
(49) Landi, B. J.; Ganter, M. J.; Schauerman, C. M.; Cress, C. D.; Raffaelle, R. P. Lithium ion capacity of single wall carbon nanotube paper electrodes. *J. Phys. Chem. C* **2008**, *112*, 7509−7515.
(50) Yang, Z.; Wu, H.-Q.; Simard, B. Charge−discharge characteristics of raw acid-oxidized carbon nanotubes. *Electrochem. Commun.* **2002**, *4*, 574−578.
(51) Oktaviano, H. S.; Yamada, K.; Waki, K. Nano-drilled multiwalled carbon nanotubes: characterizations and application for LIB anode materials. *J. Mater. Chem.* **2012**, *22*, 25167−25173.
(52) Shimoda, H.; Gao, B.; Tang, X.; Kleinhammes, A.; Fleming, L.; Wu, Y.; Zhou, O. Lithium intercalation into opened single-wall carbon nanotubes: storage capacity and electronic properties. *Phys. Rev. Lett.* **2001**, *88*, 015502.
(53) Satoh, A.; Takami, N.; Ohsaki, T. Electrochemical intercalation of lithium into graphitized carbons. *Solid State Ionics* **1995**, *80*, 291−298.
(54) Kaskhedikar, N. A.; Maier, J. Lithium storage in carbon nanostructures. *Adv. Mater.* **2009**, *21*, 2664−2680.
(55) Yoo, E.; Kim, J.; Hosono, E.; Zhou, H.-s.; Kudo, T.; Honma, I. Large reversible Li storage of graphene nanosheet families for use in rechargeable lithium ion batteries. *Nano Lett.* **2008**, *8*, 2277−2282.
(56) Wu, Z.-S.; Ren, W.; Xu, L.; Li, F.; Cheng, H.-M. Doped graphene sheets as anode materials with superhigh rate and large capacity for lithium ion batteries. *ACS Nano* **2011**, *5*, 5463−5471.

DOI: 10.1021/acsami.5b04864
ACS Appl. Mater. Interfaces 2015, 7, 17441−17449